Materials Science & Engineering A 973 (2026) 150712

Contents lists available at ScienceDirect

Materials Science & Engineering A

journal homepage: www.elsevier.com/locate/msea

Synergistic optimization of elastocaloric effect and fatigue life in NiTi shape memory alloys via pretraining-coupled aging treatment

Tianyi Hu [a], Xiaoxian Zhang [a,*], Yanju Liu [a,b], Jinsong Leng [a,**]

[a] School of Astronautics, Harbin Institute of Technology, Harbin, 150001, China
[b] Suzhou Research Institute, Harbin Institute of Technology, Suzhou, 215100, China

ARTICLE INFO

Keywords:
NiTi shape memory alloy
Elastocaloric effect
Fatigue life
Microstructural reconstruction
Synergistic strengthening mechanism

ABSTRACT

Elastocaloric cooling based on NiTi shape memory alloys offers a promising alternative to conventional vapor compression refrigeration, yet the enhancement of elastocaloric and fatigue properties remains a critical challenge. In this work, a novel pretraining coupled low-temperature aging strategy is proposed to achieve synergistic optimization of these properties. For the $Ni_{50.3}Ti_{49.7}$ alloy, multiple pretraining schemes and aging conditions are investigated and the strengthening mechanism is discussed. The optimal coupled treatment is identified as cyclic pretraining to 10% strain for 5 cycles, followed by aging at 623 K for 120 min. Compared with the as-received specimen, this processing route achieves 19.3% increase in the initial adiabatic temperature change, 2.1-fold extension in fatigue life, and 50% reduction in the degradation rate of adiabatic temperature change during cyclic loading. Multiscale characterization is employed to elucidate the underlying mechanisms. The structure-property relationship is established by correlating the microstructural evolution induced by pretraining and aging treatment with the macroscopic performance changes in elastocaloric effect and fatigue life. The coupled treatment is found to reconstruct the microstructure through grain refinement with optimized crystallographic orientation, the development of stable dislocation networks and dense martensite. These insights demonstrate that by synergistically integrating multiple strengthening mechanisms through pretraining-coupled aging treatment, the trade-off between elastocaloric performance and fatigue durability in single-route processing can be effectively overcome, providing a feasible design strategy for high-performance NiTi-based elastocaloric cooling systems.

1. Introduction

Refrigeration is a critical infrastructure for ensuring food safety and industrial production in modern society. With rising living standards and intensifying global warming, the United Nations Environment Programme predicts that global demand for cooling will more than triple by 2050 [1]. Nevertheless, the refrigeration market is dominated by traditional vapor compression refrigeration that relies on chemical refrigerants with extremely high global warming potential [2,3]. The leakage or improper disposal of these refrigerants results in the direct emission of potent greenhouse gases [4]. Meanwhile, the electricity consumption of related refrigeration equipment accounts for ~20% of global electricity consumption [1,5]. As global refrigeration demand continues to expand, the challenges related to carbon emissions and energy consumption will become even more severe in the future. For solving this predicament, various industries are actively seeking new energy-saving and environmentally friendly refrigeration solutions [6–8].

Elastocaloric cooling technology based on latent heat of solid-state phase transformation has attracted widespread attention due to its environmental friendliness and high theoretical energy efficiency [9–11]. Benefiting from the high latent heat density, it can theoretically achieve efficient refrigeration cycles with low environmental burden. Among numerous candidate materials for elastocaloric cooling, NiTi shape memory alloys (SMAs) stand out as a preferred choice because of their advantages, such as large recoverable strain and high adiabatic temperature change [12,13]. In recent years, they have been adopted by various refrigeration prototypes [14–16]. However, the commercialization of this material is limited by its core performance indicators, namely elastocaloric performance and fatigue durability [17–20]. Given

* Corresponding author.
** Corresponding author.
E-mail addresses: xiaoxian@hit.edu.cn (X. Zhang), lengjs@hit.edu.cn (J. Leng).

https://doi.org/10.1016/j.msea.2026.150712
Received 19 May 2026; Received in revised form 22 June 2026; Accepted 4 July 2026
Available online 6 July 2026

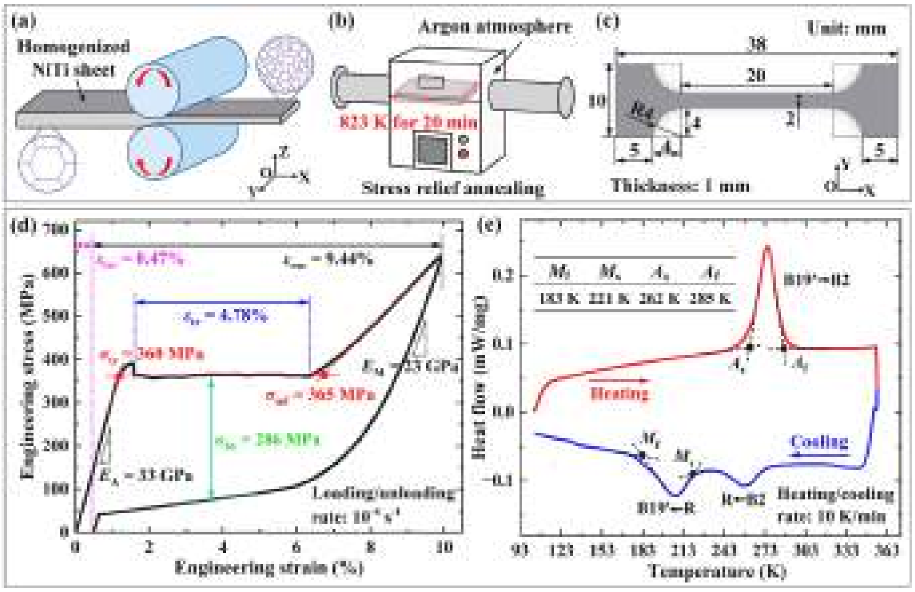

Fig. 1. Fabrication process and functional characteristics of the NiTi alloy: (a) Schematic diagram of cold-rolling process; (b) Stress relief annealing under argon atmosphere; (c) Geometry of the machined flat dog-bone specimen; (d) Engineering stress-strain curve at room temperature under loading and unloading; (e) DSC curve showing phase transformation behavior.

the high maturity of the traditional vapor compression refrigeration, the elastocaloric cooling technology are required to achieve higher elastocaloric performance and longer fatigue life to compete with established benchmarks.

Pretraining has been developed to address the reliability challenges of NiTi SMAs under high-stress and long-life service conditions [21–24]. Through controlled cyclic loading, pretraining is an effective method to adjust the functional performance of NiTi alloys. Atli et al. [25] and Saikrishna et al. [26] reported that NiTi alloys with appropriate training can exhibit more stable superelastic response and longer fatigue life in subsequent cycles. Tušek et al. [27] demonstrated that an initial pre-strain of 10% followed by cycling at the unloading plateau with adiabatic temperature changes of ~8 K in tensile-loaded NiTi plates, representing a ~60% improvement in temperature change compared to the ~5 K achieved under standard conditions. However, the mechanisms responsible for the improved performance were not fully characterized. To address this gap, Wang et al. [28] proposed a method of applying 1900 MPa overstress training to NiTi tubes, achieving an adiabatic temperature drop of ~11 K and a performance coefficient of ~55. They attributed this enhanced functional performance to the formation of near-saturated dislocation networks and residual martensite nanodomains. Although previous studies have advanced the understanding of pretraining effects, the application of pretraining in elastocaloric cooling of NiTi SMAs remains insufficiently explored and requires further investigation.

By tailoring the aging temperature and time, the microstructure of NiTi SMAs can be altered, which in turn influences the stress-induced martensitic transformation (SIMT) behavior [29–33]. Properly designed aging treatments have been demonstrated to increase the adiabatic temperature change and enhance the reversibility of phase transformations. Zhang et al. [34] enhanced the elastocaloric response of NiTi SMAs by inducing the formation of nanoscale Ni_4Ti_3 precipitates by aging treatment. Xu et al. [35] pointed out that coarsened nanoscale precipitates tend to introduce local stress concentrations, accelerating plastic damage accumulation and deteriorating cyclic stability of the material. Apart from the traditional aging processes, innovative thermal strategies have become a viable approach to improve the properties of NiTi alloys. Chen et al. [36] recovered the performance degradation of NiTi SMA caused by dislocation accumulation and residual martensite formation during cycling by intermittent thermal healing strategy. While these studies mainly focused on enhancing elastocaloric response or functional recovery, the improvement of fatigue resistance has received less attention. Therefore, it is necessary to develop strategies that can simultaneously enhance elastocaloric and fatigue properties in NiTi SMAs and to elucidate the underlying microscopic mechanisms for establishing universal design principles.

In this work, a novel strategy combining pretraining and aging treatment to synergistically optimize the elastocaloric effect and fatigue life of NiTi SMAs is proposed. Multiple sets of pretraining schemes and aging conditions are designed, and in-situ infrared thermography is utilized to monitor the elastocaloric response of the material during cyclic loading. Based on experimental data regarding adiabatic temperatures and cycle numbers, the pretraining-coupled aging treatment route for maximizing the elastocaloric and fatigue properties is determined. Furthermore, electron backscatter diffraction (EBSD) and transmission electron microscopy (TEM) are employed to characterize the as-received, single pretraining, single low-temperature aging and pretraining-coupled aging treatment state of the material. By correlating macroscopic mechanical and thermal behavior with microstructural evolution, the synergistic strengthening mechanism is elucidated.

2. Experiments

2.1. Material and specimen preparation

The NiTi ingot was homogenized at 1173 K for 12 h in an argon atmosphere and subsequently water-quenched. Next, the homogenized ingot was forged and hot-rolled into a sheet with ~20% thickness reduction reserved for further deformation processing. This sheet was cold-rolled to a final thickness of 1 mm, as shown in Fig. 1a. Then, stress relief annealing (Fig. 1b) was conducted at 823 K for 20 min in an annealing furnace under argon atmosphere to remove the residual stress introduced by cold rolling. Flat dog-bone specimens were machined from the NiTi sheet by low-speed wire electrical discharge machining, with their axial direction aligned parallel to the rolling direction of the sheet. The gauge size of the specimens was 20 mm (length) × 2 mm (width) × 1 mm (thickness), and more detailed dimensions are provided in Fig. 1c. To eliminate the surface damage and mitigate stress concentration induced by the cutting process, the specimen surfaces were progressively ground using SiC abrasive papers from coarse to fine grits,

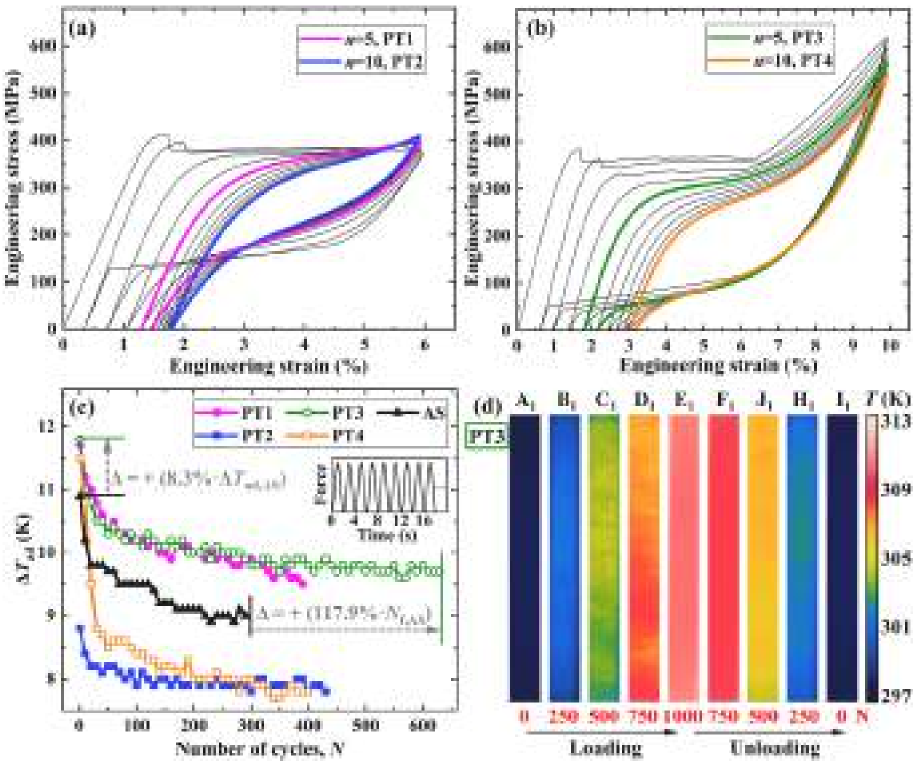

Fig. 2. Cyclic pretrainings and their effects on elastocaloric and fatigue properties: (a, b) Engineering stress-strain curves of the specimens pretrained to 6% strain for 5 cycles (PT1) and 10 cycles (PT2), to 10% strain for 5 cycles (PT3) and 10 cycles (PT4); (c) Evolution of the adiabatic temperature change ΔT_{ad} for the pretraining specimens (PT1-4) and the AS specimen during fatigue cycling N; (d) Infrared thermography images of the PT3 specimen's gauge section captured at $N = 200$.

followed by mechanical polishing to achieve a smooth surface suitable for mechanical testing. The chemical composition of the alloy was measured to be $Ni_{50.3}Ti_{49.7}$ (at.%) by energy-dispersive X-ray spectroscopy analysis.

2.2. Experimental details

The superelastic behavior of the NiTi sheet was evaluated through uniaxial tensile loading-unloading tests conducted at room temperature. Specimens were loaded to 10% strain and then completely unloaded at a constant strain rate of 1×10^{-4} s^{-1}. The resulting engineering stress-strain curve is shown in Fig. 1d. The phase transformation behavior was investigated by differential scanning calorimetry (DSC) using a Netzsch DSC 300 Caliris Classic instrument. For the DSC measurements, a cylindrical sample with dimensions of 4 mm (diameter) × 1 mm (height) was extracted from the NiTi alloy sheet. This sample was first held at 103 K for 5 min, then heated to 353 K at a rate of 10 K/min and held for 5 min, followed by cooling back to 103 K at the same rate in nitrogen atmosphere.

Fig. 1e shows the DSC curve of the NiTi alloy. During heating, a single pronounced endothermic peak appears, corresponding to the phase transformation from B19' martensite to B2 austenite, in which the austenitic start and finish temperatures are determined as $A_s = 262$ K and $A_f = 285$ K, respectively. As the temperature drops, two exothermic peaks can be observed. The first weak peak corresponds to the transformation from the parent B2 austenite phase to the intermediate R phase, while the second peak is associated with the subsequent transformation from the R phase to the B19' martensite. The martensitic transformation starts at $M_s = 221$ K and finishes at $M_f = 183$ K. Because all experiments were conducted at room temperature higher than A_f, the alloy primarily maintains its austenitic state before loading.

Stress-controlled fatigue tests were carried out at room temperature with a loading frequency of 0.5 Hz. The tests were conducted under a minimum stress of 0 N and a maximum stress of 1000 N until fracture of the specimens. Prior to these fatigue tests, selected specimens were subjected to cyclic pretraining with different cycle numbers under the strain rate of 1×10^{-4} s^{-1}. Additionally, some specimens were undertaken low-temperature aging treatment under nitrogen protection using a TJZ furnace. The specific pretraining and aging parameters will be described in the next section. During fatigue loading, a TN460 infrared thermal camera was used for in-situ temperature monitoring. The camera was mounted vertically above the gauge section of the specimen via a tripod, enabling thermal images to be captured synchronously with the mechanical process. The specimen surfaces monitored by the camera were coated with matte black paint to increase surface emissivity.

The microstructures of the tested specimens were characterized using EBSD (TESCAN MAGNA equipped with an accelerating voltage range of 0.05-30 kV) and TEM (Talos F200X equipped with an accelerating voltage of 200 kV). EBSD samples were prepared by sequential mechanical polishing of the specimen surface, followed by 30 min of vibratory polishing using a BUEHLER VibroMet system to remove the deformation layer induced by mechanical processing and obtain a high-quality mirror-like surface. Thin foils for TEM were prepared by electrolytic twin-jet thinning to ensure uniform thickness and minimize preparation artifacts.

3. Results and discussion

3.1. Processing strategy for enhanced elastocaloric effect and extended fatigue life

Fig. 1d presents the uniaxial tensile stress-strain curves of the NiTi specimen at room temperature. The initial linear segment corresponds to the elastic deformation of austenite. Upon reaching an applied stress of ~360 MPa, the austenite begins to transform into martensite, leading to the formation of a transformation plateau. Here, $\sigma_{tr} = 360$ MPa denotes the transformation start stress, while $\sigma_{mf} = 365$ MPa represents the martensite finish stress, and the associated transformation strain

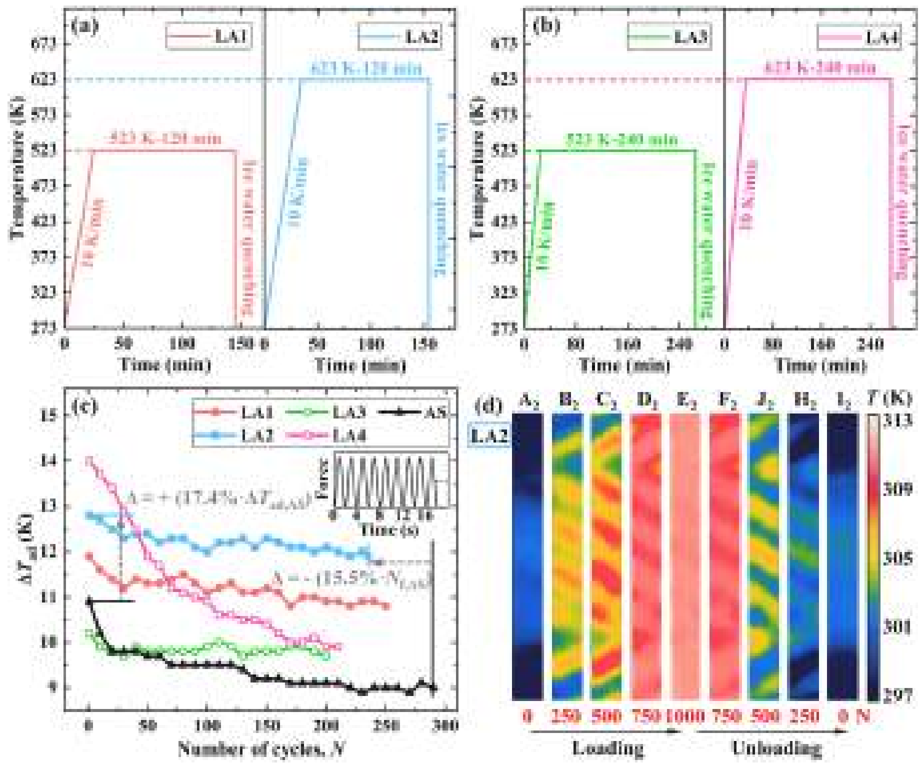

Fig. 3. Low-temperature aging treatments and their effects on elastocaloric and fatigue properties: (a, b) Heat treatment diagrams of the specimens aged under 120 min at 523 K (LA1) and 623 K (LA2), under 240 min at 523 K (LA3) and 623 K (LA4); (c) Evolution of the adiabatic temperature change ΔT_{ad} for the aging specimens (LA1-4) and the AS specimen during fatigue cycling N; (d) Infrared thermography images of the LA2 specimen's gauge section captured at $N = 200$.

$\varepsilon_{tr} = 4.78\%$. The nearly horizontal plateau with weak stress fluctuation reflects that the transformation interface moves easily, implying a stable transformation process [37,38]. The stress hysteresis $\sigma_{hy} = 286$ MPa, defined as the difference between the average transformation plateau stresses in loading and unloading, represents the energy dissipation during the forward and reverse transformations [39]. The elastic moduli of austenite and martensite, determined from the slope of the initial linear loading segment and the linear unloading segment after transformation completion, are $E_A = 33$ GPa and $E_M = 23$ GPa, respectively. The recoverable strain $\varepsilon_{rec} = 9.44\%$ suggests that most of the deformation originates from reversible SIMT rather than irreversible plastic mechanisms such as slip or twinning [40]. The irreversible strain $\varepsilon_{irr} = 0.47\%$ demonstrates nearly complete recovery of martensite variants upon unloading and minimal dislocation accumulation. In general, the large recoverable strain, low irreversible strain and well-defined hysteresis loop collectively indicate the outstanding superelasticity of this NiTi alloy at room temperature.

To systematically investigate the effects of pretraining amplitude and cycling number, four pretraining schemes were designed, as shown in Fig. 2a and b. The specimens were pretrained to 6% strain for 5 cycles (PT1) and 10 cycles (PT2), and to 10% strain for 5 cycles (PT3) and 10 cycles (PT4), aiming to identify the optimal pretraining path. The stress and strain are engineering stress and strain. With increasing cycling number, the transformation plateaus gradually shift downward. For the 6% strain condition (Fig. 2a), the transformation start stress decreases from 373 MPa in the first cycle to 324 MPa after 5 cycles and further to 296 MPa after 10 cycles. A similar trend is observed for the 10% strain condition (Fig. 2b), where the transformation start stress drops from 358 MPa in the first cycle to 282 MPa after 5 cycles and further to 218 MPa after 10 cycles. This reduction in the transformation start stress is attributed to the accumulation of residual dislocations and retained martensite variants during the cycling process, which lowers the driving force required for subsequent transformations [41]. The downward plateau shift becomes more pronounced under the higher 10% strain condition. The transformation start stress decreases by 20.6% across 10 cycles under 6% strain, whereas a much larger reduction of 39.1% occurs under 10% strain. Meanwhile, the stress hysteresis decreases markedly with cycling. Under the 6% strain condition (Fig. 2a), it decreases from 228 MPa in the first cycle to 152 MPa after 5 cycles and further to 104 MPa after 10 cycles, corresponding to a total reduction of 54.4%. Under the 10% strain condition (Fig. 2b), the stress hysteresis decreases from 279 MPa in the first cycle to 225 MPa after 5 cycles and further to 161 MPa after 10 cycles, totaling a reduction of 42.3%. Notably, the reduction in stress hysteresis is greater at 6% strain than at 10% strain. This may be attributed to the insufficient stabilization of the martensitic transformation at 6% strain. The unsaturated dislocation density and internal stress fields allow for continuous microstructural reorganization, leading to hysteresis decay as transformation pathways evolve. In contrast, the 10% strain condition establishes a near-saturated state at the early cycles. Consequently, the further microstructural evolution during subsequent cycling is constrained, ultimately leading to a smaller decrease at higher strain levels [22,28].

The evolution of adiabatic temperature change (ΔT_{ad}) during fatigue cycling is compared between the pretraining specimens (PT1-PT4) and the as-received (AS) specimen, as shown in Fig. 2c. During the initial stage, the ΔT_{ad} decreases sharply in all cases. All pretraining schemes successfully extend the fatigue life (N_f) relative to the AS specimen. Among them, the PT4 specimen shows a 117.9% increase in N_f compared with the AS specimen. For the specimens subjected to 10 cycles of pretraining (PT2 and PT4), the ΔT_{ad} remains lower than that of the AS specimen throughout cycling. By contrast, the specimens pretrained for 5 cycles (PT1 and PT3) maintain higher ΔT_{ad} over the entire fatigue process. The initial ΔT_{ad} increases from 10.9 K for the AS specimen to 11.7 K for PT1 and 11.8 K for PT3, corresponding to the improvements of 7.3% and 8.3%, respectively. Near fatigue fracture, the ΔT_{ad} remains at 9.5 K for PT1 and 9.7 K for PT3, both of which are higher than 9.0 K for the AS specimen, representing increases of 5.6% and 7.8%, respectively. To further quantify the degradation behavior

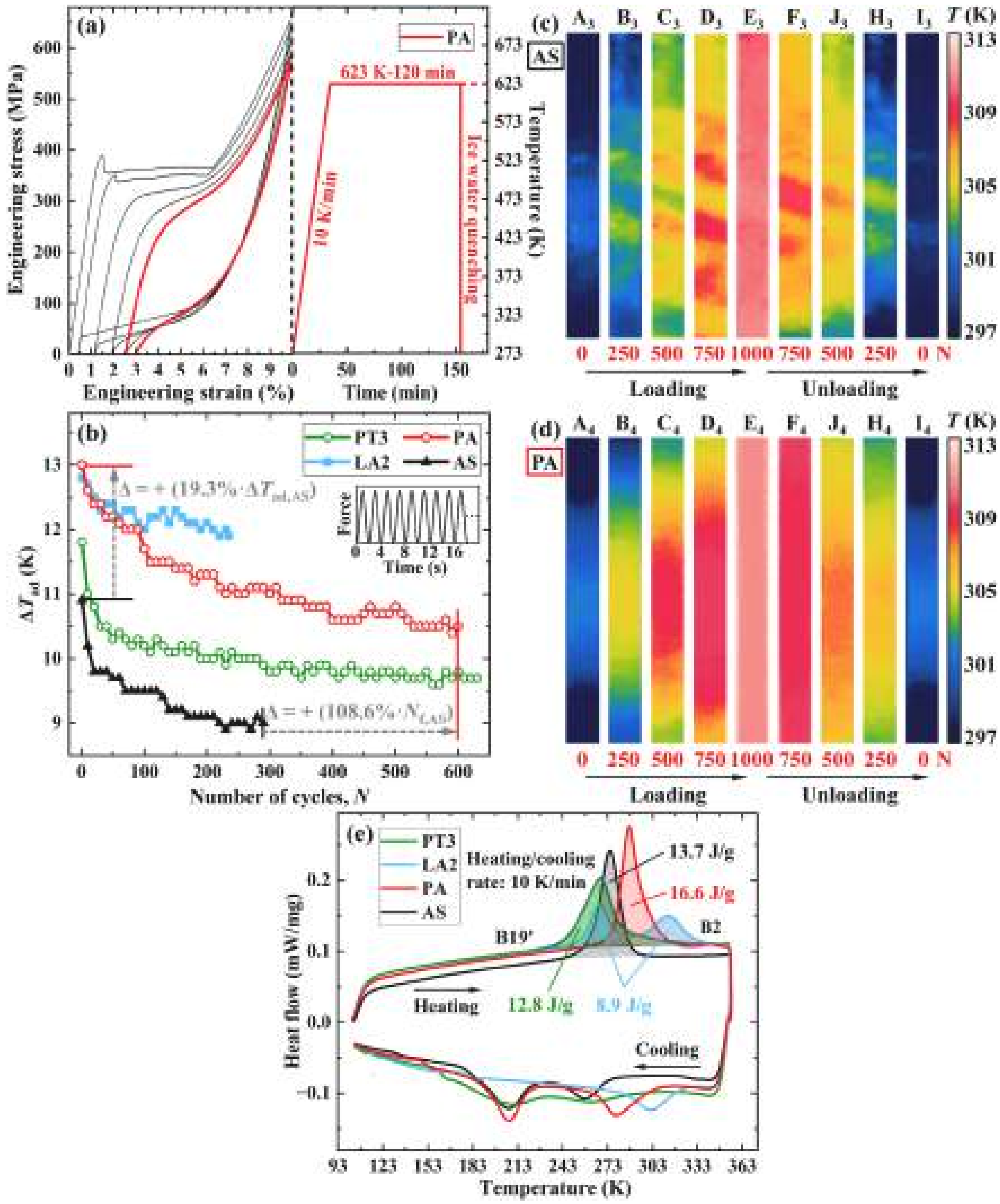

Fig. 4. Effect of pretraining-coupled aging treatment on elastocaloric and fatigue properties: (a) Schematic of the two-step processing route involving cyclic pretraining to 10% strain for 5 cycles followed by aging at 623 K for 120 min (the PA specimen); (b) Evolution of the adiabatic temperature change ΔT_{ad} for the specimens (PA, PT3, LA2 and AS) during fatigue cycling N; (c, d) Infrared thermography images of the AS and PA specimens' gauge section captured at $N = 200$; (e) DSC curves showing phase transformation behavior of the AS, PT3, LA2 and PA specimens, including the transformation enthalpy change ΔH during heating process.

during cycling, the average ΔT_{ad} degradation rates are evaluated for the entire cycling until fatigue fracture. The AS specimen shows a degradation rate of ~0.0066 K/cycle. PT1 and PT3 show reduced degradation rates of ~0.0055 and ~0.0033 K/cycle, respectively, indicating enhanced functional stability against cyclic loading. Although PT2 shows the lowest degradation rate of ~0.0023 K/cycle, its overall ΔT_{ad} level remains at a relatively low level. Moreover, PT4 exhibits the highest degradation rate of ~0.0092 K/cycle, reflecting poor stability of the elastocaloric response. Among all pretraining conditions, PT3 stands out as the optimal choice, achieving improvements in both N_f and ΔT_{ad}, while simultaneously lowering the degradation rate of ΔT_{ad}. Fig. 2d displays infrared thermography images of the gauge section of the PT3 specimen captured during one complete loading-unloading cycle at $N = 200$, providing a direct visualization of its elastocaloric response. During the loading process (A_1-E_1), SIMT releases heat and the specimen temperature rises. During the unloading process (E_1-I_1), the reverse transformation absorbs heat and the specimen cools [42]. The temperature field is relatively uniform during the cycle, indicating that cyclic pretraining enables a large part of the gauge section to participate in the reversible phase transformation during cycling, which is essential for achieving repeatable and stable elastocaloric cooling.

The low-temperature aging treatment was introduced to evaluate its influence on the functional properties of the NiTi alloy under cyclic loading. As illustrated in Fig. 3a and b, four aging conditions were employed, including 523 K/120 min (LA1), 623 K/120 min (LA2), 523 K/240 min (LA3) and 623 K/240 min (LA4), each followed by ice-water quenching. This matrix of conditions was deliberately constructed to decouple the respective contributions of aging temperature and holding time. Fig. 3c presents the evolution of ΔT_{ad} during fatigue cycling for the aged specimens (LA1-4) in comparison with the AS specimen. Compared with the AS specimen, all aged specimens exhibit a clear reduction in N_f. LA1 and LA2 show reductions of 13.8% and 15.5%, respectively, whereas larger decreases are observed for LA3 and LA4, reaching 29.7% and 25.2%, respectively. This trend indicates that extending the holding time from 120 to 240 min at the same aging temperature is unfavorable for the fatigue durability of this NiTi alloy under the present aging conditions. Regarding the elastocaloric response, aging treatment generally elevates the initial ΔT_{ad} relative to the AS specimen. LA2 and LA4 exhibit initial ΔT_{ad} values of 12.8 K and 13.4 K, corresponding to increases of 17.4% and 22.9%, respectively, while LA1 reaches 11.9 K, representing an improvement of 9.2%. LA3 records the lowest initial ΔT_{ad} of 10.2 K among all aged specimens, which is 6.4% below that of the AS specimen, indicating that this aging condition does not improve the initial elastocaloric output. LA3 displays an average degradation rate of ~0.0025 K/cycle. LA4 experiences the most severe degradation, dropping by 3.5 K from 13.4 K to 9.9 K over 217 cycles, yielding the highest ΔT_{ad} degradation rate of ~0.0161 K/cycle. LA1 and LA2 show intermediate degradation rates of ~0.0044 K/cycle and ~0.0037 K/cycle, respectively. Among all aging conditions, LA2 demonstrates the most balanced overall performance, ranking second in N_f, initial ΔT_{ad} and average ΔT_{ad} degradation rate. Accordingly, aging at 623 K for 120 min provides a suitable processing window to improve the elastocaloric output while maintaining acceptable fatigue resistance.

Fig. 3d presents infrared thermography images of the gauge section of the LA2 specimen captured during a complete loading-unloading cycle at $N = 200$. As shown in these images, the evolution of transient temperature field during SIMT differs markedly from that observed in the PT3 specimen (Fig. 2d). While the PT3 specimen displays a nearly uniform temperature field, the LA2 specimen exhibits distinct band-like temperature patterns oriented at ~45° to the loading axis. These bands are commonly referred to as Lüders-like bands, a deformation localization phenomenon of NiTi alloys under tension [43]. In this mode, the SIMT proceeds through the propagation of Lüders-like bands, where the deformation is characterized by significant inhomogeneities within the strain fields along the specimen length. During cyclic loading, the active regions swept by the moving fronts of these bands experience large local strain oscillations and transient thermal effects. This concentrated activity promotes localized cyclic phase transformation and energy dissipation, accelerating microstructural damage accumulation and reducing fatigue life [44,45]. This phenomenon is consistent with the shorter N_f of the LA2 specimen compared with the AS specimen in Fig. 3c.

To overcome the limitations of single processing routes in optimizing the functional performance of NiTi alloys, a pretraining-coupled aging treatment process was designed by combining cyclic pretraining and low-temperature aging along their respective optimal pathways. As illustrated in Fig. 4a, the specimen was first subjected to cyclic pretraining at room temperature by loading to a strain of 10% followed by complete unloading, repeated five times. Subsequently, low-temperature aging treatment was conducted at 623 K for 120 min, followed by ice-water quenching. Fig. 4b shows the evolution of ΔT_{ad} during fatigue loading for the pretraining-coupled aging specimen (PA) in comparison with the AS specimen, the solely pretrained specimen (PT3), and the solely aged specimen (LA2). In terms of N_f, the PA specimen sustains 605 cycles before failure, which is more than twice that of the AS specimen with 290 cycles. Regarding the elastocaloric response, the PA specimen achieves the highest initial ΔT_{ad} of 13.0 K among all conditions. When normalized by N_f, the average ΔT_{ad} degradation rate of the PA specimen is ~0.0041 K/cycle, higher than that of LA2 at ~0.0037 K/cycle and PT3 at ~0.0033 K/cycle, yet lower than that of the AS specimen at ~0.0066 K/cycle. In general, the pretraining-coupled aging treatment combines the advantages of both single-route processes. That is, the PA specimen exhibits 108.6% increase in N_f relative to the AS specimen, while maintaining higher ΔT_{ad} values throughout the entire life, with improvements of 19.3% at the beginning and 16.7% near fracture. Meanwhile, its average ΔT_{ad} degradation rate is 37.9% lower than that of the AS specimen. Compared with the PT3 specimen that underwent only pretraining, the PA specimen achieves 10.2% higher initial ΔT_{ad} and retains 8.2% higher ΔT_{ad} near fracture, while exhibiting similar N_f with a difference of 4.3%. This demonstrates that the subsequent aging step elevates the elastocaloric output without significantly reducing the fatigue durability gained from pretraining. Compared with the LA2 specimen that underwent only aging treatment, the PA specimen shows 146.9% increase in N_f and exhibits a slightly higher initial ΔT_{ad}, but the ΔT_{ad} near fracture is lower with a reduction of 11.8%. This indicates that while aging treatment alone can effectively improve the elastocaloric effect, it comes at the expense of fatigue durability. By integrating the enhancing effect of pretraining and aging treatment, the PA specimen successfully overcomes this limitation, achieving a superior balance between elastocaloric performance and cyclic durability than neither single-route process can offer alone.

Infrared thermography images of the AS and PA specimens captured during a complete loading-unloading cycle at $N = 200$ are presented in Fig. 4c and d, respectively. For the AS specimen, the temperature field shows obvious non-uniformity (Fig. 4c). Discontinuous temperature variation regions can be observed with blurred boundaries compared with the temperature field of the LA2 specimen in Fig. 3d. The phase transformation preferentially concentrates within these localized regions, accompanied by unstable and irregular propagation of the transformation fronts. By contrast, the PA specimen displays a more uniform temperature field at the same cycle number (Fig. 4d). This shift from localized (Fig. 4c) to uniform (Fig. 4d) transformation behavior reflects the effectiveness of the coupled treatment in regulating the propagation mode of SIMT at macroscopic scale. The resulting uniformity of the thermal response implies a larger proportion of the material participates more synchronously in the elastocaloric effect, which is beneficial for enhancing overall cooling efficiency [39,46,47]. Moreover, the specimens in Fig. 2d and 4d characterized by more uniform temperature field evolution demonstrate longer fatigue lives than those in Fig. 3d and 4c with localized temperature fields. These observations indicate a positive correlation between the uniformity of temperature field and N_f [48].

Fig. 4e presents the DSC curves of the AS, PT3, LA2 and PA specimens, revealing the effect of different processing routes on the phase transformation behavior of the NiTi alloy. The transformation enthalpy ΔH is obtained by integrating the endothermic peaks related to the thermally induced reverse transformation from B19' martensite to B2 austenite during heating. Compared with the AS specimen, the PT3 specimen shows a decrease in A_f to ~279 K, indicating that cyclic pretraining lowers the temperature required to complete the reverse transformation from B19' martensite to B2 austenite. Meanwhile, the ΔH of the PT3 specimen is ~12.8 J/g, slightly lower than that of the AS specimen. The LA2 specimen exhibits two endothermic peaks during heating. This behavior indicates the involvement of an intermediate transformation process. For this specimen, the summed area of the two endothermic peaks gives a ΔH value of ~8.9 J/g. Notably, the A_f of the LA2 specimen shifts markedly upward to ~330 K, which is well above room temperature. Therefore, the LA2 specimen is not be fully transformed into the B2 austenitic state before mechanical loading. For the

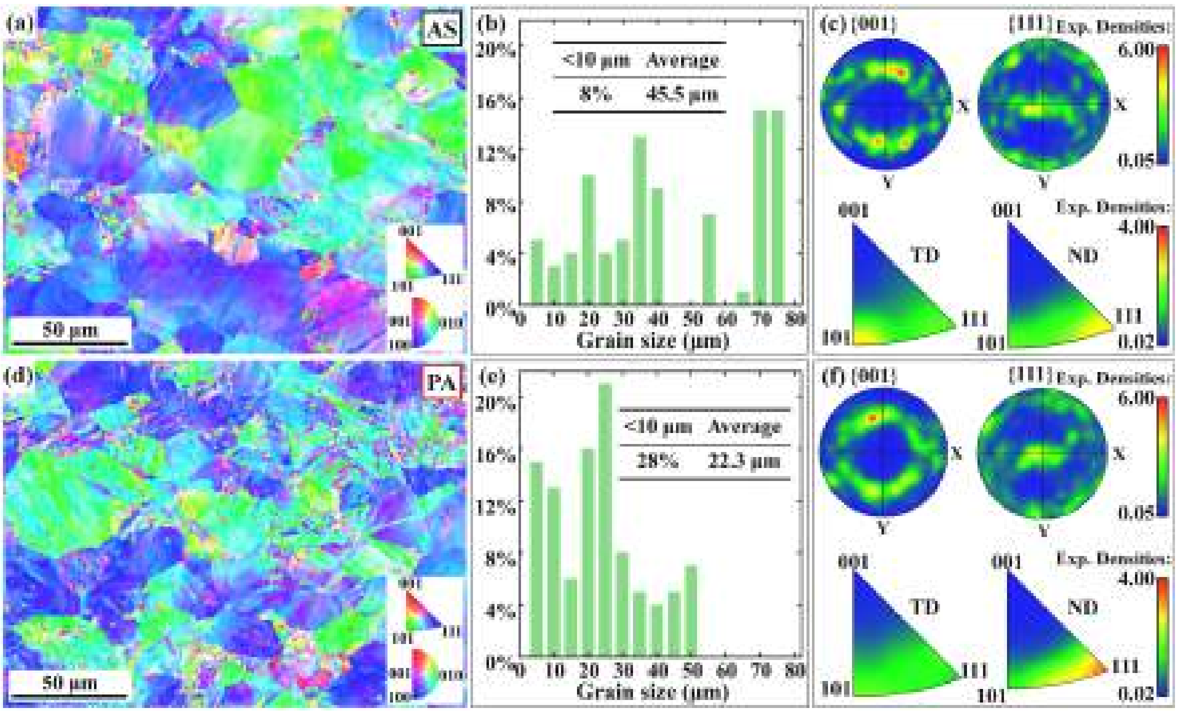

Fig. 5. EBSD characterizations of the AS (a-c) and PA (d-f) specimens: (a, d) IPF maps; (b, e) Grain size distributions; (c, f) Pole figures and corresponding inverse pole figures.

PA specimen, A_f is ~296 K, and ΔH during DSC heating reaches ~16.6 J/g. This indicates that the coupled treatment adjusts the reverse transformation temperature to a range close to the testing temperature, while increasing the latent heat. Such a transformation state may facilitate the activation of SIMT under mechanical loading.

3.2. *Influence of pretraining-coupled aging treatment on microstructure*

The microstructural evolution of the specimens after pretraining-coupled aging treatment and its relation to the improvement of macroscopic elastocaloric and fatigue properties were investigated using multiscale characterization by EBSD and TEM through a comparison between the AS and PA specimens. The EBSD results in Fig. 5 show clear

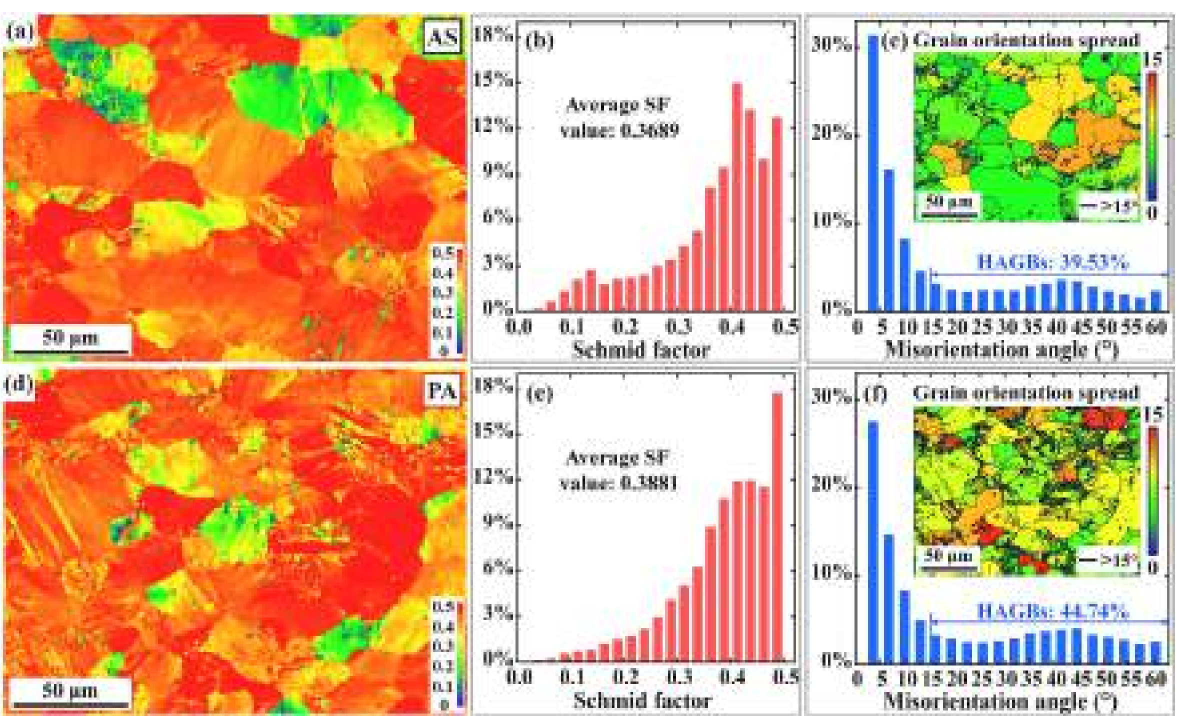

Fig. 6. EBSD characterizations of the AS (a-c) and PA (d-f) specimens: (a, d) Schmid factor maps; (b, e) Schmid factor distributions; (c, f) Grain orientation spread maps and misorientation angle distributions.

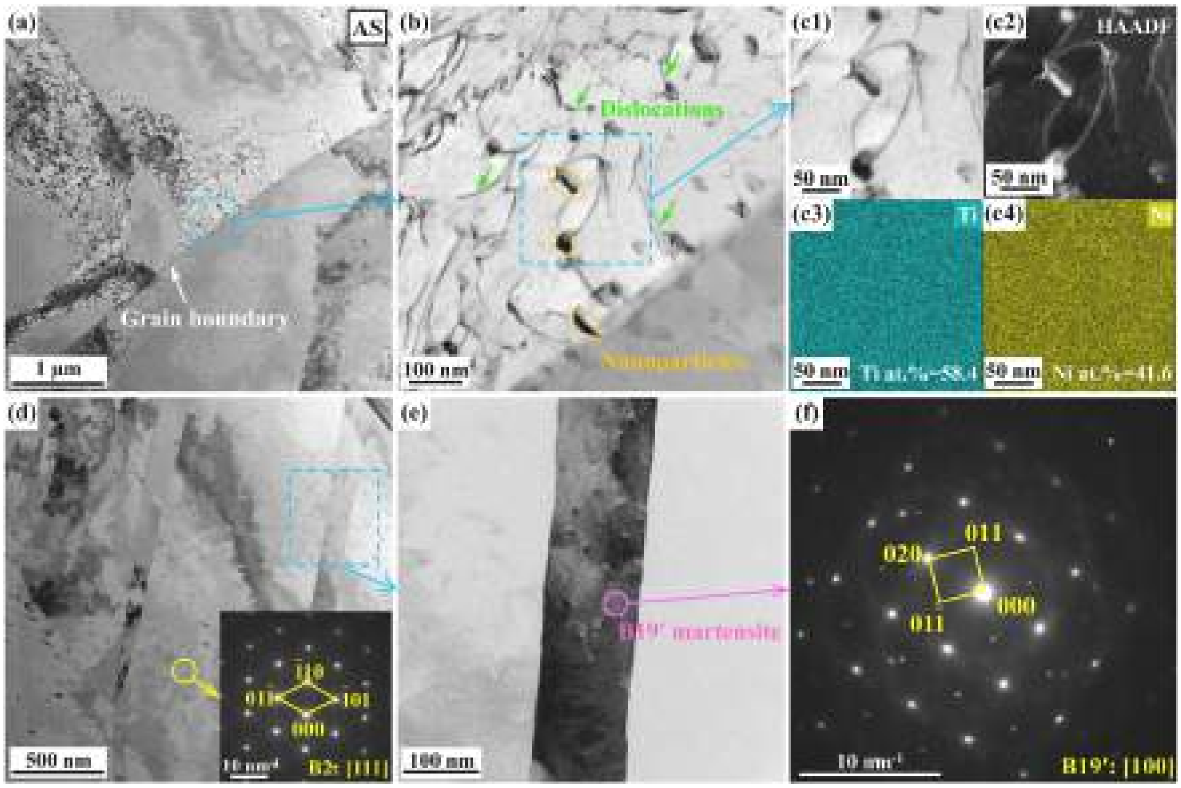

Fig. 7. TEM observations of the AS specimen: (a) Microstructural morphology near the grain boundary; (b) Dislocations and nanoparticles; (c1) Magnified image of the selected region in (b); (c2) HAADF-STEM image corresponding to (c1); (c3, c4) STEM-EDS maps of Ti and Ni; (d) Martensite in B2 matrix, inset is SAED pattern indexed to B2 phase; (e) Magnified image of B19' martensite in (d); (f) SAED pattern taken from the region marked in (e), indexed to B19' phase.

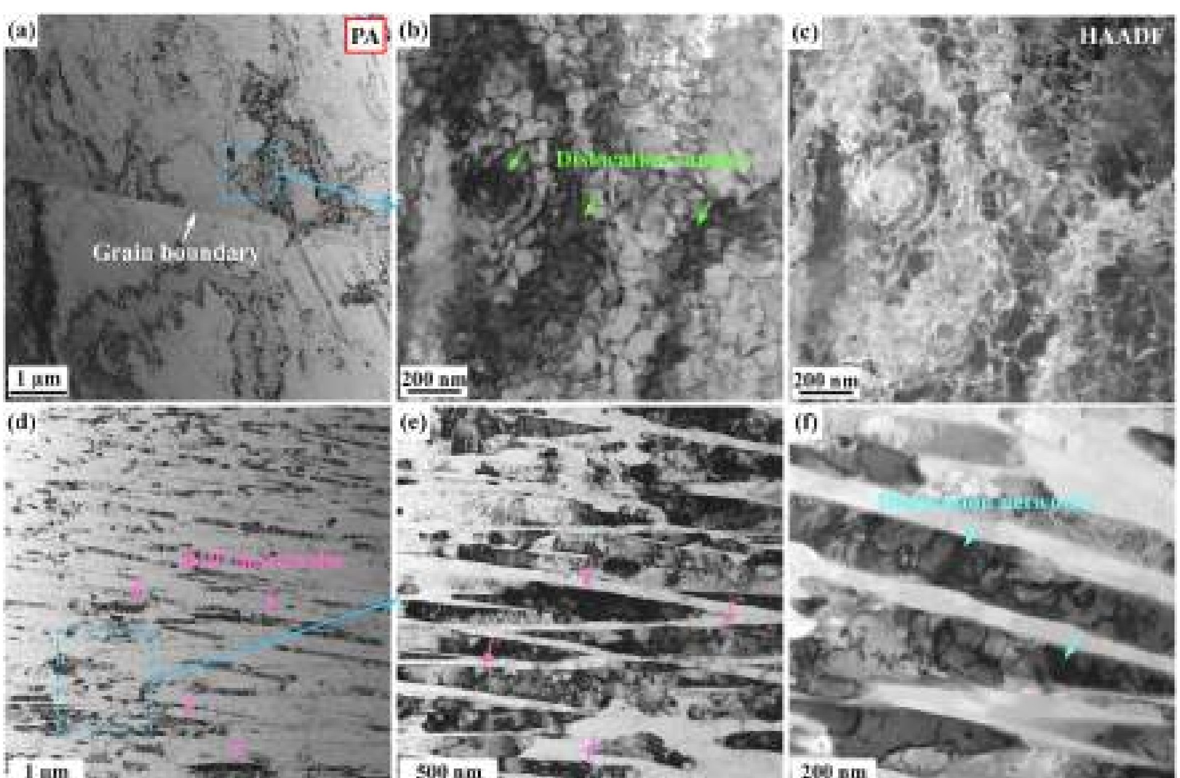

Fig. 8. TEM observations of the PA specimen: (a) Microstructural morphology near the grain boundary; (b) Magnified image of the selected region in (a) showing dislocation tangles; (c) HAADF-STEM image corresponding to (b); (d) B19' martensite in the matrix; (e) Magnified image of B19' martensite in (d); (f) Dislocation networks within the martensite.

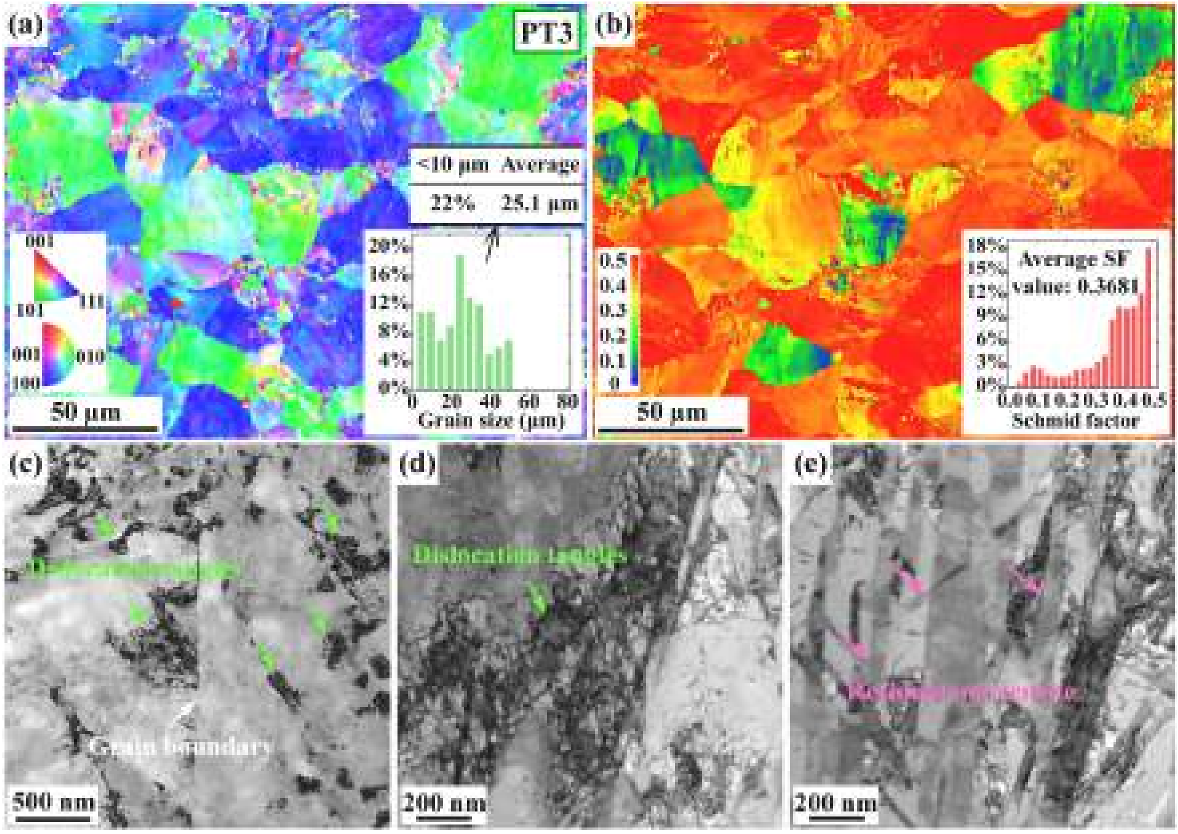

Fig. 9. Microstructural characterizations of the PT3 specimens ((a, b) observed by EBSD and (c-e) observed by TEM): (a) IPF map with corresponding grain size distribution; (b) Schmid factor map with corresponding SF value distribution; (c) Morphology near the grain boundary; (d) Dislocation tangles; (e) Residual martensite.

differences in their grain morphologies and crystal orientations. Fig. 5a and d presents the inverse pole figure (IPF) maps of the AS and PA specimens, respectively. In the AS specimen, the microstructure consists of coarse grains with intragranular orientation variations, where orientation changes are relatively smooth within individual grains. By contrast, the PA specimen displays considerably finer grains, accompanied by stronger intragranular orientation gradients. The grain size distributions in Fig. 5b and e confirm the refinement induced by the coupled treatment. Here, the grain sizes are quantified using the equivalent circular diameter, and the distributions are presented as area-weighted fractions. The AS specimen has an average grain size of ~45.5 μm, with ~8% of grains below 10 μm. The distribution of the PA specimen shifts toward smaller sizes, in which the average grain size decreases to ~22.3 μm and the proportion of grains below 10 μm increases to ~28%. According to the Hall-Petch relationship, grain refinement generally increases material strength, which reduces plastic strain accumulation during cyclic loading and improve fatigue resistance [47]. The B2 pole figures and inverse pole figures of the AS and PA specimens are presented in Fig. 5c and f, respectively. After the coupled treatment, the peak intensity in the {001} pole figures rise from 5.63 to 5.75, and the pole distribution becomes more concentrated. The maximum orientation density near ⟨111⟩ in the ND inverse pole figures increases from 2.81 to 3.46. These results suggest that the pretraining-coupled aging treatment moderately strengthens the texture and promotes a redistribution of crystallographic orientations.

A crystallographic comparison between the AS and PA specimens is presented in Fig. 6. The Schmid factor (SF) maps for the AS and PA specimens are shown in Fig. 6a and d, respectively. In the AS specimen, most of the grains appear in orange to red colors, reflecting relatively high SF values, while a small proportion of grains forms green regions with lower SF values. By contrast, the SF map of the PA specimen displays a more homogeneous color distribution. The statistical histograms in Fig. 6b and e quantify this trend. The SF distribution of the AS specimen has an average value of ~0.3689, whereas that of the PA specimen becomes more concentrated and shifts toward higher values, with the average SF value increasing to ~0.3881. Despite this value exhibits a modest increase, the strong orientation sensitivity of SIMT in NiTi alloys enables a larger proportion of grains to reach the critical transformation condition. This promotes a transition from localized Lüders-like band propagation to a more synchronized transformation mode. Consequently, the phase transformation proceeds more uniformly across the gauge section, as evidenced by the more homogeneous temperature field in the PA specimen (Fig. 4d) compared to the AS specimen (Fig. 4c) [49–51].

Fig. 6c and f shows the grain orientation spread (GOS) maps and misorientation angle distributions (MADs) of the AS and PA specimens, respectively. The GOS map of the AS specimen is mainly green and yellow, indicating generally low average GOS values and intragranular orientation spread with small lattice distortion. This reflects a low internal strain state retained after the cold-rolling and stress-relief annealing process. In contrast, the PA specimen exhibits more yellow and locally red regions, representing high average GOS values in many grains. The MAD shows that the fraction of high-angle grain boundaries (HAGBs, >15°) is ~39.53% in the AS specimen and increases to ~44.74% in the PA specimen. The higher HAGBs fraction imposes stronger obstacles to dislocation motion. Furthermore, HAGBs can act as preferential nucleation sites for SIMT, facilitating a more uniform phase transformation at macroscopic scale [52].

Further TEM observations were performed on the AS and PA specimens, as shown in Figs. 7 and 8 respectively. Fig. 7a presents the microstructure near the grain boundary, in which most areas within the interior of grains appear clean, but some local areas exhibit a noticeable

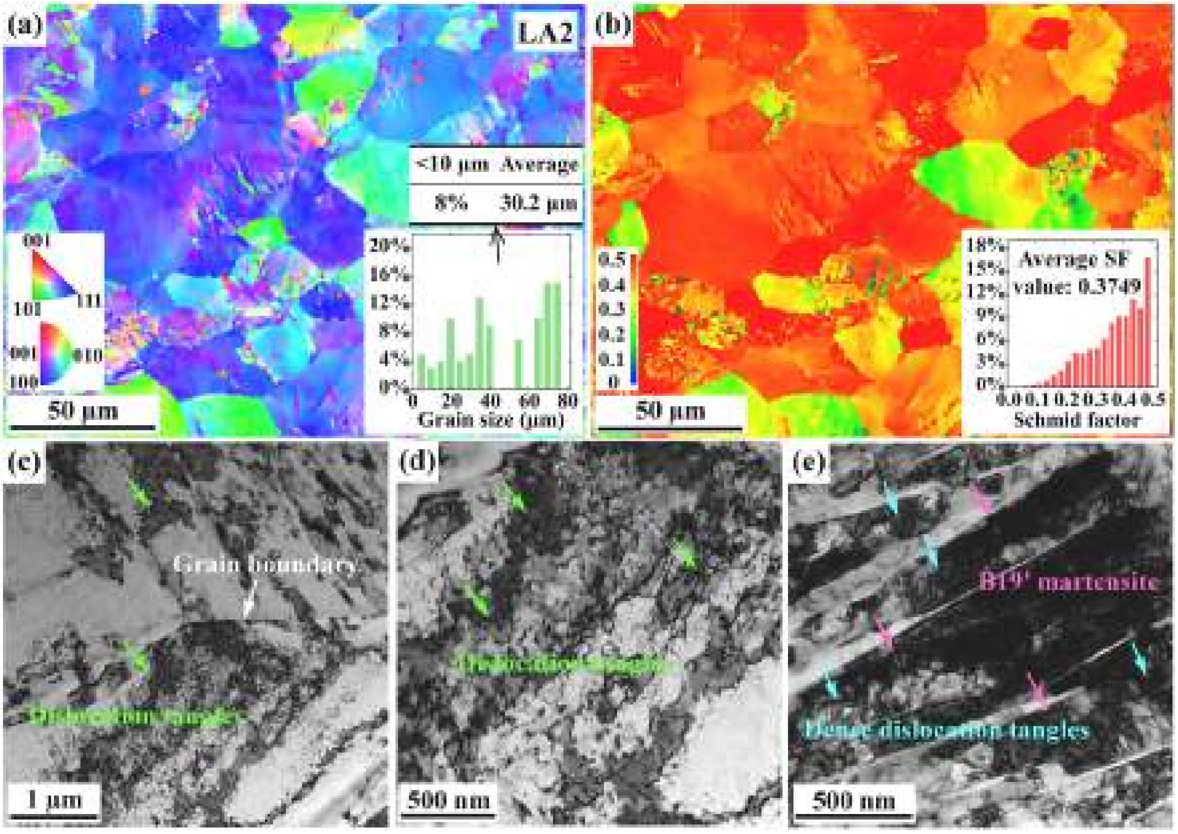

Fig. 10. Microstructural characterizations of the LA2 specimens ((a, b) observed by EBSD and (c-e) observed by TEM): (a) IPF map with corresponding grain size distribution; (b) Schmid factor map with corresponding SF value distribution; (c) Morphology near the grain boundary; (d) Dislocation tangles; (e) B19' martensite and dense dislocation tangles within the martensite.

density of dislocations. Higher-magnification image of the selected region near the grain boundary (Fig. 7b) reveals intertwined dislocations accompanied by nanoparticles. The nanoparticles range in size from several nanometers to ~20 nm. Fig. 7c1 is a magnified bright-field image of the selected region in Fig. 7b, and the corresponding HAADF-STEM image is shown in Fig. 7c2. The STEM-EDS elemental maps (Fig. 7c3 and 7c4) reveal a nearly uniform distribution of both Ti and Ni without obvious compositional segregation. Quantitative data shows an atomic composition of Ti with ~58.4 at.% and Ni with ~41.6 at.%. This Ti-rich composition, combined with the absence of resolvable second-phase diffraction spots, suggests that these nanoparticles represent early-stage coherent Ti-rich clusters or short-range ordered structures [34,53,54]. Their compositional and structural fluctuations are insufficient to produce clear diffraction contrast, yet are capable of inducing local lattice distortions. In addition, martensite structures are observed within another grain, as shown in Fig. 7d. The inset SAED pattern from the surrounding matrix confirms the B2 austenite phase. The magnified image of the selected region (Fig. 7e) and the corresponding SAED pattern (Fig. 7f) can be indexed to the B19' martensite phase, with a maximum martensite width of ~130 nm.

TEM observations of the PA specimen are shown in Fig. 8. Relative to the AS specimen, dislocation tangles can be seen in the microstructural morphology near the grain boundary (Fig. 8a) and the magnified image of the selected region (Fig. 8b). The corresponding HAADF-STEM image in Fig. 8c further confirms the formation of dislocation-entangled structures in the PA specimen. In addition, numerous B19' martensite structures are visible in the matrix (Fig. 8d). The magnified image of the selected region in Fig. 8e shows that these martensite structures are roughly aligned and closely spaced, indicating that their morphology is constrained by the directional internal stress field introduced by pretraining. The maximum martensite width is ~300 nm, ~2.3 times that of the AS specimen. Fig. 8f reveals the well-developed dislocation networks within the martensite phase, reflecting the complex defect state of the martensitic phase after the coupled treatment. This microstructure stands in sharp contrast to the isolated and sparsely distributed residual martensite observed in the AS specimen (Fig. 7d). The changed martensitic morphology allows the macroscopic transformation strain to be distributed over a larger number of microscopic transformation units, resulting in a more cooperative transformation process throughout the material [38,52].

3.3. Mechanism underlying the optimization of elastocaloric and fatigue properties

To clarify the effect of pretraining alone on the microstructure, the PT3 specimens subjected to cyclic pretraining to 10% strain for 5 cycles were jointly characterized by EBSD (Fig. 9a and b) and TEM (Fig. 9c–e). The IPF map and corresponding grain size distribution in Fig. 9a shows an average grain size of ~25.1 μm with ~22% of grains below 10 μm, indicating that cyclic pretraining alone induces 44.8% reduction in average grain size compared with the AS specimen. The SF map with corresponding SF value distribution in Fig. 9b indicates an average SF value of ~0.3681, comparable to that of the AS specimen but lower than that of the PA specimen. Fig. 9c presents the microstructural morphology near the grain boundary in the PT3 specimen. On both sides of the grain boundary, localized clusters of dislocations can be seen, as marked by green narrows. A closer examination of these dislocation-rich regions at higher magnification (Fig. 9d) shows that the dislocations are entangled. Relative to the scattered dislocations in the AS specimen (Fig. 7b), the PT3 specimen possesses higher dislocation density, indicating that pretraining introduces dislocation structures serving as the nucleation sites for subsequent phase transformation [41]. Fig. 9e shows

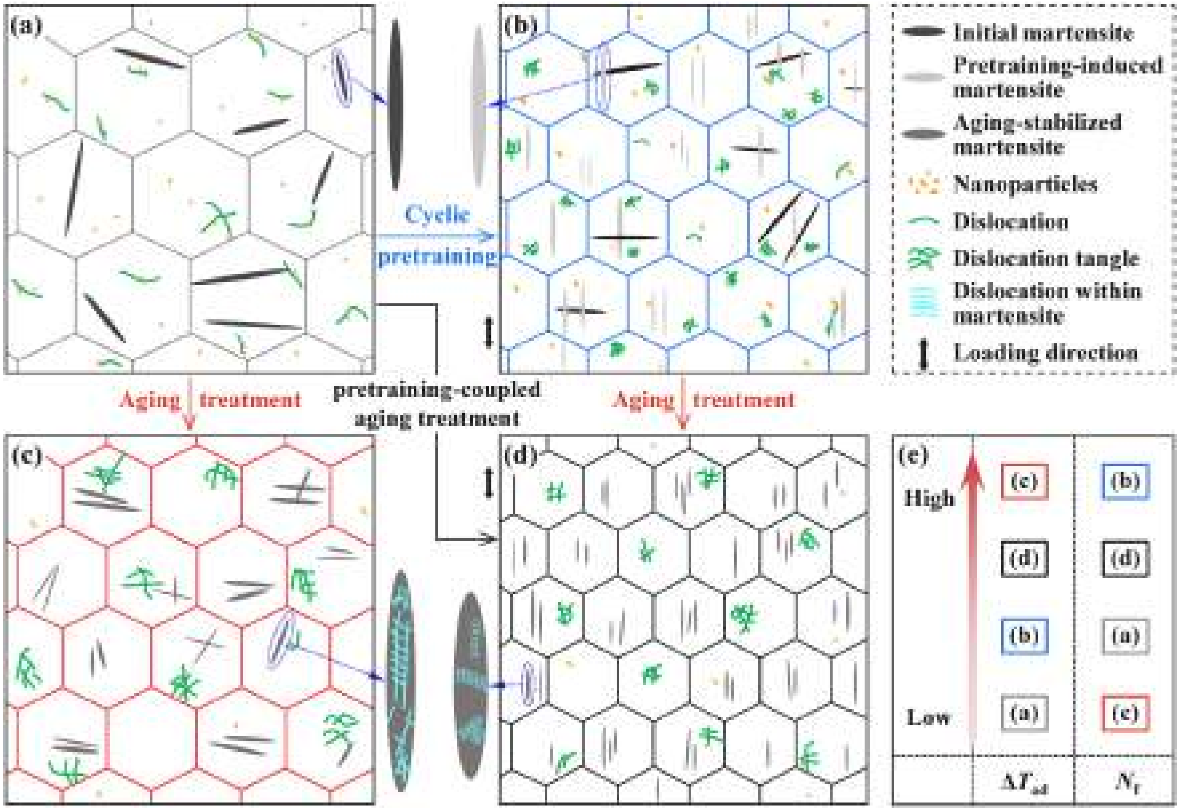

Fig. 11. Schematic illustration of microstructural evolution in the $Ni_{50.3}Ti_{49.7}$ alloy under different processing routes in this study: (a) As-received state; (b) Cyclic pretraining; (c) Aging treatment; (d) Pretraining-coupled aging treatment; (e) Ranking of the adiabatic temperature change ΔT_{ad} and fatigue life N_f for these four material states.

residual martensite with blurred interfaces, representing martensite variants that are not fully recovered to austenite upon unloading. The presence of such residual martensite, together with the accumulated dislocation structures, introduces local heterogeneity into the internal stress state, causing the cyclic transformation behavior in subsequent loading cycles to gradually deviate from the behavior of the initial cycle.

The microstructure of the LA2 specimens subjected only to aging at 623 K for 120 min was examined by EBSD (Fig. 10a and b) and TEM (Fig. 10c–e). The IPF map and corresponding grain size distribution in Fig. 10a show an average grain size of ~30.2 μm, with ~8% of grains smaller than 10 μm. The grain size is reduced by ~33.6% compared with the AS specimen, but remains larger than those of the PT3 and PA specimens. Therefore, the most significant grain refinement is achieved in the PA specimen. Fig. 10b shows the SF map with corresponding SF value distribution, indicating an average SF value of ~0.3749, which is higher than those of the AS and PT3 specimens but still lower than that of the PA specimen. As shown in Fig. 10c and d, dislocation tangles are present near the grain boundary, and localized region of martensite aggregation can be observed. In contrast to the PT3 specimen (Fig. 9c), where the dislocations are distributed in numerous small clusters, the LA2 specimen exhibits more extensive dislocation-entangled regions in the matrix. At higher magnification in Fig. 10e, B19' martensite structures are clearly resolved, with a maximum width of ~260 nm and dense dislocation tangles occupying the interior of the martensite [21,35].

Fig. 11 schematically illustrates the microstructural evolution of the $Ni_{50.3}Ti_{49.7}$ alloy under different processing routes and its correlation with elastocaloric and fatigue properties. The microstructure of the as-received state at room temperature is shown in Fig. 11a. A small amount of isolated initial B19' martensite is embedded in the B2 matrix, representing in black color. Dislocations are sparsely distributed and locally aggregated within the grains, and nanoscale Ti-rich particles are dispersed in the matrix, with some interacting with nearby dislocations. The alloy exhibits the largest average grain size among all conditions. Relatively, the as-received state exhibits the lowest ΔT_{ad} and a short N_f. After cyclic pretraining, the microstructural evolution is depicted in Fig. 11b. Stress-induced martensite variants are generated along the loading direction. These pretraining-induced martensite variants are represented in light gray to distinguish them from the initial martensite originally present in the material. Dislocation density increases significantly, forming multiple localized tangles within the grains. Furthermore, cyclic loading induces significant grain refinement. The effect of grain refinement and dislocation strengthening enables the pretraining specimen to achieve the longest fatigue life in this study, while the limited crystallographic optimization results in only a modest improvement in elastocaloric performance.

The microstructure of the low-temperature aging state is illustrated in Fig. 11c. The aging-stabilized B19' martensite form within localized intragranular regions, representing in dark gray color. High-density dislocation tangles are observed within the B19' martensite and the surrounding B2 austenite matrix. The pretraining-coupled aging treatment state is shown in Fig. 11d. The stabilized dense martensite within the grains aggregates with a near-uniform morphology constrained by the pretraining strain field, enabling more cooperative phase transformation. Dislocation networks are developed inside the martensite, contributing additional resistance to irreversible deformation during cyclic loading. Under this condition, the grains are refined, and the crystallographic orientation distribution becomes more concentrated. Meanwhile, the average SF value increases, suggesting that more grains are favorably oriented for SIMT under loading. The ranking of ΔT_{ad} and N_f for these four conditions is presented in Fig. 11e. The pretraining-coupled aging treatment ranks second in both ΔT_{ad} and N_f among all four conditions. Overall, the coupled process is not a simple superposition of mechanical and thermal treatment effects. Instead, it integrates refined grains and stable dislocation networks in a synergistic manner, reconstructing an optimized microstructure that can simultaneously enhance elastocaloric performance and fatigue durability, overcoming the inherent trade-off encountered in single-route processing.

4. Conclusions

In this work, a pretraining-coupled aging treatment strategy was proposed to synergistically optimize the elastocaloric effect and fatigue life of NiTi SMAs. The effects of pretraining parameters and aging conditions on the elastocaloric response and fatigue durability were systematically investigated, and the microstructural evolution induced by each individual and coupled treatment was characterized by EBSD and TEM. The underlying synergistic strengthening mechanism was also elucidated. The main conclusions of this study are summarized as follows:

(1) Compared with the AS specimen, cyclic pretraining alone increases N_f by ~117.9% and reduces the average ΔT_{ad} degradation rate by ~50%, but provides only modest improvement in the elastocaloric output by ~8.3%, with the optimal pretraining condition identified as 10% strain for 5 cycles. Low-temperature aging alone increases the initial ΔT_{ad} by ~17.4% and lowers the average ΔT_{ad} degradation rate by ~44%, while reducing N_f by ~15.5%, with the optimal aging condition determined as 623 K for 120 min.

(2) The pretraining-coupled aging treatment simultaneously increases the initial ΔT_{ad} by ~19.3% and extends N_f by ~108.6%, with the average ΔT_{ad} degradation rate reduced by ~37.9%. The coupled treatment refines the average grain size by ~51% and elevates the average SF value by ~5.2%, promotes dense dislocation tangles and networks within B2 matrix and B19′ martensite, as well as stabilizes residual martensite at multiple intragranular sites with a more uniform morphology, enhancing phase transformation coordination and reversibility.

(3) The synergistic strengthening mechanism results from the integrated contributions of distinct microstructural features across multiple scales. The enhanced elastocaloric effect is attributed to the optimized crystallographic orientation, which allows a larger proportion of grains to reach the critical transformation condition under the same applied stress. The improved fatigue durability is governed by grain refinement impeding dislocation motion, high-density dislocation tangles pinning irreversible slip and providing nucleation sites for SIMT. The closely spaced martensite promotes a more uniform phase transformation, reducing local strain localization and stabilizing ΔT_{ad} during cyclic loading.

CRediT authorship contribution statement

Tianyi Hu: Conceptualization, Data curation, Formal analysis, Investigation, Visualization, Writing – original draft. **Xiaoxian Zhang:** Funding acquisition, Supervision, Validation, Writing – review & editing. **Yanju Liu:** Supervision, Validation, Writing – review & editing. **Jinsong Leng:** Conceptualization, Funding acquisition, Resources, Writing – review & editing.

Declaration of competing interest

The authors declare that they have no known competing financial interests or personal relationships that could have appeared to influence the work reported in this paper.

Acknowledgment

This work was supported by the science foundation of national key laboratory of science and technology on advanced composites in special environments [grant number JZKJW20250018-04]. The authors acknowledge Yang Jiao and Zhengbo Zhang (Center of Analysis and Measurement, Harbin Institute of Technology) for their assistance with EBSD and TEM measurements.

Data availability

Data will be made available on request.

References

[1] United Nations Environment Programme, Global cooling watch 2025: the free degrees. https://www.unep.org/resources/global-cooling-watch-2025, 2025.
[2] X. She, L. Cong, B. Nie, G. Leng, H. Peng, Y. Chen, X. Zhang, T. Wen, H. Yang, Y. Luo, Energy-efficient and -economic technologies for air conditioning with vapor compression refrigeration: a comprehensive review, Appl. Energy 232 (2018) 157–186.
[3] N. Kumma, S.S.H. Kruthiventi, Current status of refrigerants used in domestic applications: a review, Renew. Sustain. Energy Rev. 189 (2024) 114073.
[4] X. Zhang, Y. Li, A review of recent research on hydrofluoroolefin (HFO) and hydrochlorofluoroolefin (HCFO) refrigerants, Energy 311 (2024) 133423.
[5] L.T. Biardeau, L.W. Davis, P. Gertler, C. Wolfram, Heat exposure and global air conditioning, Nat. Sustain. 3 (1) (2019) 25–28.
[6] J. Tušek, K. Engelbrecht, D. Eriksen, S. Dall′Olio, J. Tušek, N. Pryds, A regenerative elastocaloric heat pump, Nat. Energy 1 (10) (2016) 16134.
[7] M.O. McLinden, J.S. Brown, R. Brignoli, A.F. Kazakov, P.A. Domanski, Limited options for low-global-warming-potential refrigerants, Nat. Commun. 8 (1) (2017) 14476.
[8] H. Niu, X. Liu, B. Wang, W. Shi, Development, research and policy status of logistics cold storage in the context of carbon neutrality: an overview, Energy Build. 320 (2024) 114606.
[9] C. Aprea, A. Greco, A. Maiorino, C. Masselli, Solid-state refrigeration: a comparison of the energy performances of caloric materials operating in an active caloric regenerator, Energy 165 (2018) 439–455.
[10] M. Imran, X. Zhang, Reduced dimensions elastocaloric materials: a route towards miniaturized refrigeration, Mater. Des. 206 (2021) 109784.
[11] S. Wang, Y. Shi, Y. Li, H. Lin, K. Fan, X. Teng, Solid-state refrigeration of shape memory alloy-based elastocaloric materials: a review focusing on preparation methods, properties and development, Renew. Sustain. Energy Rev. 187 (2023) 113762.
[12] J. Shi, D. Han, Z. Li, L. Yang, S.-G. Lu, Z. Zhong, J. Chen, Q.M. Zhang, X. Qian, Electrocaloric cooling materials and devices for zero-global-warming-potential, high-efficiency refrigeration, Joule 3 (5) (2019) 1200–1225.
[13] A. Amadi, Advancing engineering frontiers with NiTi shape memory alloys: a multifaceted review of properties, fabrication, and application potentials, J. Alloys Compd. 976 (2024) 173227.
[14] R. Snodgrass, D. Erickson, A multistage elastocaloric refrigerator and heat pump with 28 K temperature span, Sci. Rep. 9 (1) (2019) 18532.
[15] Y. Chen, Y. Wang, W. Sun, S. Qian, J. Liu, A compact elastocaloric refrigerator, Innovation 3 (2) (2022) 100205.
[16] G. Zhou, L. Zhang, Z. Li, P. Hua, Q. Sun, S. Yao, Achieving kilowatt-scale elastocaloric cooling by a multi-cell architecture, Nature 639 (8053) (2025) 87–92.
[17] G. Eggeler, E. Hornbogen, A. Yawny, A. Heckmann, M. Wagner, Structural and functional fatigue of NiTi shape memory alloys, Mater. Sci. Eng. A 378 (1–2) (2004) 24–33.
[18] J. Chen, L. Lei, G. Fang, Elastocaloric cooling of shape memory alloys: a review, Mater. Today Commun. 28 (2021) 102706.
[19] L. Mañosa, A. Planes, Elastocaloric effect in shape-memory alloys, Shape Mem. Superelast. 10 (2) (2024) 89–98.
[20] MdI. Hossain, M.S. Rabbi, M.T. Ali, Shape memory alloys in modern engineering: progress, problems, and prospects, RSC Adv. 15 (40) (2025) 33046–33100.
[21] K. Gall, H.J. Maier, Cyclic deformation mechanisms in precipitated NiTi shape memory alloys, Acta Mater. 50 (18) (2002) 4643–4657.
[22] C.N. Saikrishna, K.V. Ramaiah, J. Bhagyaraj, Gouthama, S.K. Bhaumik, Influence of stored elastic strain energy on fatigue behaviour of NiTi shape memory alloy thermal actuator wire, Mater. Sci. Eng. A 587 (2013) 65–71.
[23] C. Maletta, E. Sgambitterra, F. Furgiuele, R. Casati, A. Tuissi, Fatigue properties of a pseudoelastic NiTi alloy: strain ratcheting and hysteresis under cyclic tensile loading, Int. J. Fatig. 66 (2014) 78–85.
[24] Z. Li, Z. Li, Y. Lu, X. Lu, L. Zuo, Enhanced elastocaloric effect and refrigeration properties in a Si-doped Ni-Mn-In shape memory alloy, J. Mater. Sci. Technol. 117 (2022) 167–173.
[25] K.C. Atli, I. Karaman, R.D. Noebe, D. Gaydosh, The effect of training on two-way shape memory effect of binary NiTi and NiTi based ternary high temperature shape memory alloys, Mater. Sci. Eng. A 560 (2013) 653–666.
[26] C.N. Saikrishna, K.V. Ramaiah, D. Paul, S.K. Bhaumik, Enhancement in fatigue life of NiTi shape memory alloy thermal actuator wire, Acta Mater. 102 (2016) 385–396.
[27] J. Tušek, A. Žerovnik, M. Čebron, M. Brojan, B. Žužek, K. Engelbrecht, A. Cadelli, Elastocaloric effect vs fatigue life: exploring the durability limits of Ni-Ti plates under pre-strain conditions for elastocaloric cooling, Acta Mater. 150 (2018) 295–307.

[28] Q. Wang, H. Yin, Q. Sun, Enhancing functional stability of NiTi tube for elastocaloric cooling through overstress training, J. Mater. Res. Technol. 30 (2024) 8906–8914.

[29] F. Jiang, Y. Liu, H. Yang, L. Li, Y. Zheng, Effect of ageing treatment on the deformation behaviour of Ti-50.9 at.% Ni, Acta Mater. 57 (16) (2009) 4773–4781.

[30] M. Moshref-Javadi, S.H. Seyedein, M.T. Salehi, M.R. Aboutalebi, Age-induced multi-stage transformation in a Ni-rich NiTiHf alloy, Acta Mater. 61 (7) (2013) 2583–2594.

[31] G. Laplanche, T. Birk, S. Schneider, J. Frenzel, G. Eggeler, Effect of temperature and texture on the reorientation of martensite variants in NiTi shape memory alloys, Acta Mater. 127 (2017) 143–152.

[32] J.D. Silva, S.C. Martins, N.I.D.A. Lopes, P.D. Resende, L.A. Santos, V.T.L. Buono, Effects of aging treatments on the fatigue resistance of superelastic NiTi wires, Mater. Sci. Eng. A 756 (2019) 54–60.

[33] X. Li, H. Chen, W. Guo, Y. Guan, Z. Wang, Q. Zeng, X. Wang, Improved superelastic stability of NiTi shape memory alloys through surface nano-crystallization followed by low temperature aging treatment, Intermetallics 131 (2021) 107114.

[34] Q. Zhang, Y. Wang, X. Xiao, J. Zhang, W. Zhang, M. Liu, B. Huang, B. Xu, C. Yu, C. Wang, Q. Wang, Improved elastocaloric effect of NiTi shape memory alloys strengthened by Ni_4Ti_3 nanoprecipitates, Acta Mater. 281 (2024) 120442.

[35] B. Xu, X. Xiao, Q. Zhang, C. Yu, D. Song, Q. Kan, C. Wang, Q. Wang, G. Kang, Enhanced cyclic stability of NiTi shape memory alloy elastocaloric materials with Ni_4Ti_3 nanoprecipitates: experiment and phase field modeling, J. Mech. Phys. Solid. 196 (2025) 106011.

[36] J. Chen, F. Liu, G. Fang, U. Ramamurty, Intermittent healing for alleviating the functional fatigue and restoration of the elastocaloric effect in superelastic NiTi shape memory alloy, J. Mater. Sci. Technol. 227 (2025) S1005030225000489.

[37] J.A. Shaw, S. Kyriakides, On the nucleation and propagation of phase transformation fronts in a NiTi alloy, Acta Mater. 45 (2) (1997) 683–700.

[38] O. Tyc, E. Iaparova, O. Molnárová, L. Heller, P. Šittner, Stress induced martensitic transformation in NiTi at elevated temperatures: martensite variant microstructures, recoverable strains and plastic strains, Acta Mater. 279 (2024) 120287.

[39] Y. Wu, E. Ertekin, H. Sehitoglu, Elastocaloric cooling capacity of shape memory alloys - role of deformation temperatures, mechanical cycling, stress hysteresis and inhomogeneity of transformation, Acta Mater. 135 (2017) 158–176.

[40] Y. Chen, O. Molnárová, O. Tyc, L. Kadeřávek, L. Heller, P. Šittner, Recoverability of large strains and deformation twinning in martensite during tensile deformation of NiTi shape memory alloy polycrystals, Acta Mater. 180 (2019) 243–259.

[41] R. Sidharth, T.B. Celebi, H. Sehitoglu, Origins of functional fatigue and reversible transformation of precipitates in NiTi shape memory alloy, Acta Mater. 274 (2024) 119990.

[42] E. Bonnot, R. Romero, L. Manosa, E. Vives, A. Planes, Elastocaloric effect associated with the martensitic transition in shape-memory alloys, Phys. Rev. Lett. 100 (12) (2008) 125901.

[43] Y. Liu, Y. Liu, J. Humbeeck, Lüders-like deformation associated with martensite reorientation in NiTi, Scr. Mater. 39 (8) (1998) 1047–1055.

[44] L. Brinson, Stress-induced transformation behavior of a polycrystalline NiTi shape memory alloy: micro and macromechanical investigations via in situ optical microscopy, J. Mech. Phys. Solid. 52 (7) (2004) 1549–1571.

[45] L. Zheng, Y. He, Z. Moumni, Lüders-like band front motion and fatigue life of pseudoelastic polycrystalline NiTi shape memory alloy, Scr. Mater. 123 (2016) 46–50.

[46] J. Chen, L. Xing, G. Fang, L. Lei, W. Liu, Improved elastocaloric cooling performance in gradient-structured NiTi alloy processed by localized laser surface annealing, Acta Mater. 208 (2021) 116741.

[47] H. Lin, P. Hua, Q. Sun, Effects of grain size and partial amorphization on elastocaloric cooling performance of nanostructured NiTi, Scr. Mater. 209 (2022) 114371.

[48] X. Ju, Z. Moumni, A. Borbély, Y. Zhang, S. Zhong, Quantification of microscale factors for fatigue failure in NiTi shape memory alloys, J. Mater. Res. Technol. 31 (2024) 1–5.

[49] K. Gall, The role of texture in tension-compression asymmetry in polycrystalline NiTi, Int. J. Plast. 15 (1) (1999) 69–92.

[50] S.C. Mao, J.F. Luo, Z. Zhang, M.H. Wu, Y. Liu, X.D. Han, EBSD studies of the stress-induced B2-B19′ martensitic transformation in NiTi tubes under uniaxial tension and compression, Acta Mater. 58 (9) (2010) 3357–3366.

[51] J. Lu, M. Aziz, H. Li, C. Zhang, Z. Huang, F. Chen, Orientation-dependent phase transformation pathways enabling superior superelastic and elastocaloric performance of NiTi alloys, Adv. Sci. 13 (12) (2026) 19606.

[52] Z. Wang, J. Chen, R. Kocich, S. Tardif, I.P. Dolbnya, L. Kunčická, J.-S. Micha, K. Liogas, O.V. Magdysyuk, I. Szurman, A.M. Korsunsky, Grain structure engineering of NiTi shape memory alloys by intensive plastic deformation, ACS Appl. Mater. Interfaces 14 (27) (2022) 31396–31410.

[53] J.X. Zhang, M. Sato, A. Ishida, On the Ti_2Ni precipitates and Guinier-Preston zones in Ti-rich Ti-Ni thin films, Acta Mater. 51 (11) (2003) 3121–3130.

[54] J. Chen, C. Zhao, S. Zhang, W. Zhang, W. Liu, L. Lei, U. Ramamurty, G. Fang, Imparting high elastocaloric cooling potential to NiTi alloy by two-step enhancements, Mater. Sci. Eng.: A 892 (2024) 146073.